nature physics

SUPPLEMENTARY INFORMATION
https://doi.org/10.1038/s41567-019-0417-8

In the format provided by the authors and unedited.

Measuring quantized circular dichroism in ultracold topological matter

Luca Asteria[1], Duc Thanh Tran[2], Tomoki Ozawa[3], Matthias Tarnowski[1,4], Benno S. Rem[1,4], Nick Fläschner[1,4], Klaus Sengstock[1,4,5]*, Nathan Goldman[2] and Christof Weitenberg[1,4]

[1]Institut für Laserphysik, Universität Hamburg, Hamburg, Germany. [2]Center for Nonlinear Phenomena and Complex Systems, Université Libre de Bruxelles, Brussels, Belgium. [3]Interdisciplinary Theoretical and Mathematical Sciences Program, RIKEN, Wako, Japan. [4]The Hamburg Centre for Ultrafast Imaging, Hamburg, Germany. [5]Zentrum für Optische Quantentechnologien, Universität Hamburg, Hamburg, Germany.
*e-mail: klaus.sengstock@physnet.uni-hamburg.de

Supplementary Information: Measuring quantized circular dichroism in ultracold topological matter

Luca Asteria,[1] Duc Thanh Tran,[2] Tomoki Ozawa,[3] Matthias Tarnowski,[1,4] Benno S. Rem,[1,4] Nick Fläschner,[1,4] Klaus Sengstock,[1,4,5,*] Nathan Goldman,[2] and Christof Weitenberg[1,4]

[1]*Institut für Laserphysik, Universität Hamburg, 22761 Hamburg, Germany*

[2]*Center for Nonlinear Phenomena and Complex Systems, Université Libre de Bruxelles, CP 231, Campus Plaine, B-1050 Brussels, Belgium*

[3]*Interdisciplinary Theoretical and Mathematical Sciences Program (iTHEMS), RIKEN, Wako, Saitama 351-0198, Japan*

[4]*The Hamburg Centre for Ultrafast Imaging, 22761 Hamburg, Germany*

[5]*Zentrum für Optische Quantentechnologien, Universität Hamburg, 22761 Hamburg, Germany*

(Dated: January 23, 2019)

DATA OF CHIRAL SPECTRA AND NUMERICAL SIMULATIONS

Figure S1 presents the chiral spectra for many Floquet frequencies, which were used in order to obtain the dichroic signal shown in Fig. 4 of the main text. These experimental spectra show the depletion rates at the reference amplitude $E_{\mathrm{sp}}^{\mathrm{ref}} = 0.006\,E_{\mathrm{r}}/a_{\mathrm{lat}}$. For comparison, we also show the spectra that were numerically calculated for our 2-band model, using the same parameters, in Fig. S2. These numerical simulations are based on the full-time dynamics of the 2-band Floquet system (see the Supplementary of Ref. [S1]); in particular, this includes the Fourier width associated with the finite spectroscopy time of 5 ms as well as the effects due to the counter-rotating terms (i.e. the effects that are neglected upon invoking the rotating-wave approximation). We note that these numerical simulations do not include the effects due to the initial population in the upper band nor the effects due to the external harmonic trap. In Fig. S3, we show similar spectra resulting from the linear shaking, and we present the corresponding numerical spectra in Fig. S4. Finally, we present the optical conductivity curves obtained from the chiral spectra in Fig. S5.

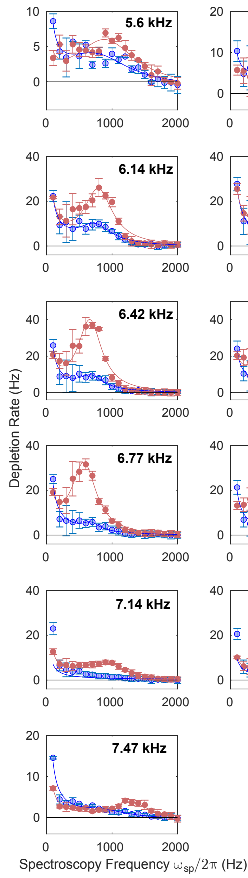

FIG. S1. **Experimental spectra for circular shaking**. Depletion rates for probing with positive chirality (red) and negative chirality (blue). The number in the subfigures states the Floquet frequency $\omega_{\mathrm{Fl}}/2\pi$. Please note the varying scale of the y-axis. All y-error bars show the error from the fit to the exponential decay.

MOMENTUM DEPENDENCE OF THE MATRIX ELEMENTS

The coupling strength of the chiral perturbation between the two Floquet bands is given by the corresponding matrix element. Fig. S6 shows these momentum-resolved matrix elements for both chiralities of the perturbation and for different Floquet frequencies corresponding to $C = 0$ and $C = 1$ regions. The coupling is very different for the two chiralities, which is - in combination with the band separation and the density of states - at the origin of the circular dichroism. The plots also explain why the depletion spectrum for positive chirality has its weight at higher frequencies than the spectrum for negative chirality for both large and small Floquet frequencies. For red-detuned Floquet frequencies, positive chirality couples most strongly at the Γ point, which corresponds

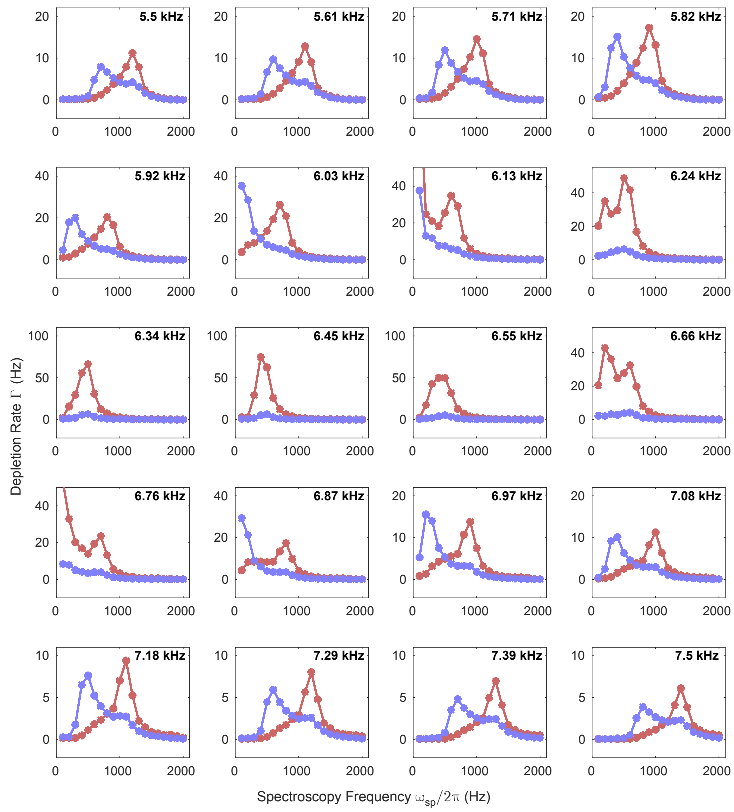

FIG. S2. **Numerical spectra for circular shaking**. Depletion rates for probing with positive chirality (red) and negative chirality (blue). The number in the subfigures states the Floquet frequency $\omega_{\mathrm{Fl}}/2\pi$.

here to large band gaps. In contrast, for blue-detuned Floquet frequencies it couples most strongly at the K point, which corresponds to the large band gaps in this regime. The Dirac points at the Γ and K point are most relevant for this discussion due to the large density of states at these band extrema. These observations can be related to the phenomenon of valley-selective coupling of circular polarized light in graphene [S11].

DISCUSSION OF SYSTEMATIC EFFECTS

An effect that might reduce the dichroism signal is the edge-state contribution, which is expected to completely compensate the bulk response in the ideal system [S2]. This effect would lead to a dichroism of opposite sign at small spectroscopy frequencies, which couple to the edge states. We do not observe such a signal in our frequency-resolved measurements and instead measure the full quantized value for the frequency-integrated differential rate. It seems that edge states do not play an important role for the spectroscopy in our harmonically trapped system. We attribute

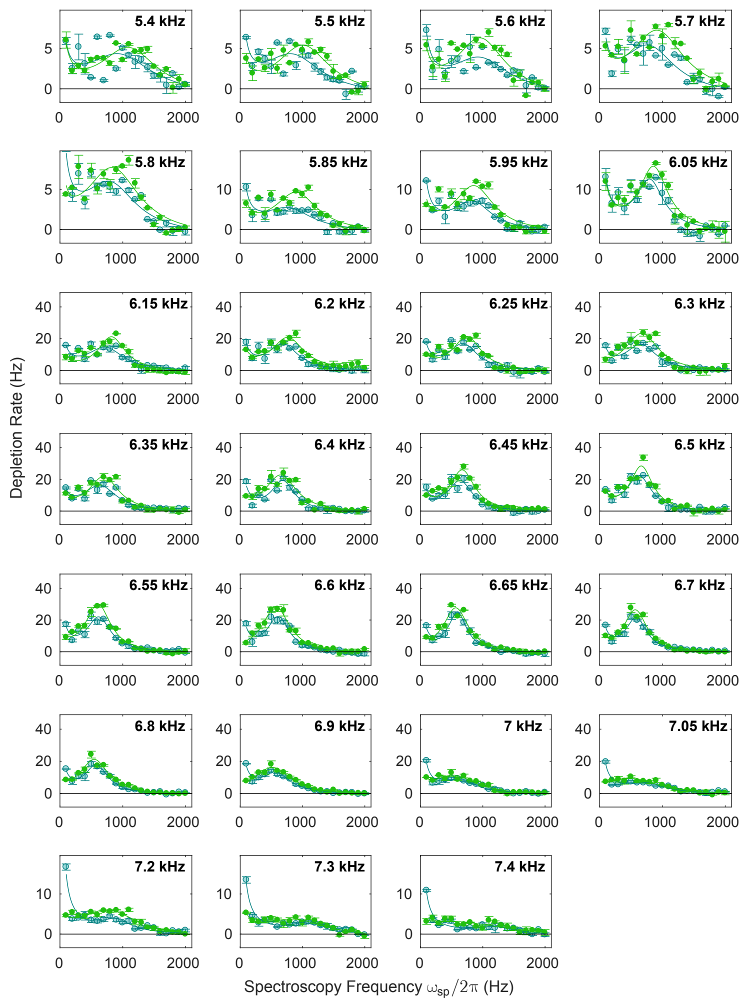

FIG. S3. **Experimental spectra for linear shaking**. Depletion rates for probing along the x direction (dark green) and the y direction (light green). The number in the subfigures states the Floquet frequency $\omega_{\mathrm{Fl}}/2\pi$. All y-error bars show the error from the fit to the exponential decay.

this to the reduced overlap between the bulk and edge states in the harmonic trap [S12, S13], and to an attenuation of the edge-states signal inherent to our band-mapping technique (the edge-states population being most probably redistributed among both Bloch bands). This is also consistent with the quantized Hall drift observed in harmonically-trapped bosonic gases [S14].

The inhomogeneous system and the dynamics induced by the external trap (about 70 Hz) washes out the momentum-dependence of the excitations [S15] (compare Fig. 2**c** of the main text). Therefore a momentum-resolved evaluation of the data, which would also reveal the Berry curvature, is not possible.

We fit the chiral spectra in Fig. 3 of the main text with a heuristic function $\Gamma_{\pm}(\omega_{\mathrm{sp}}) =$

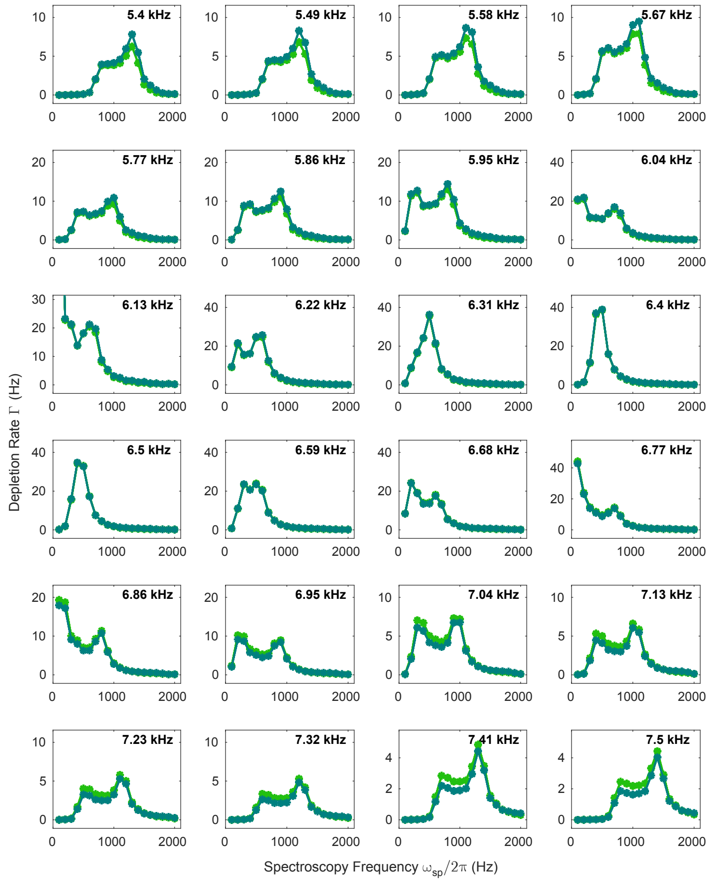

FIG. S4. **Numerical spectra for linear shaking**. Depletion rates for probing along the x direction (dark green) and the y direction (light green). The number in the subfigures states the Floquet frequency $\omega_{\mathrm{Fl}}/2\pi$.

$\frac{a}{\pi\gamma}\frac{1}{1+[(\omega_{\mathrm{sp}}-\omega_0)/\gamma]^2}+\frac{b}{\omega_{\mathrm{sp}}}+c$, composed of a Lorentzian peak of width γ at ω_0 and a $1/\omega_{\mathrm{sp}}$ term. The choice of a Lorentzian curve is motivated by the dominant role of Fourier broadening of our spectra and the rectangular spectroscopy pulse: the Lorentzian curve decays with the same power as the Fourier transform of a rectangle. The $1/\omega_{\mathrm{sp}}$ term captures an additional heating feature at low frequencies, which we attribute to the initial jump in the lattice velocity at the switch-on/off of the spectroscopy pulse. This jump necessarily appears in a realization of the circular driving with zero mean velocity and hence zero mean displacement of the lattice after one spectroscopy period. For linear spectroscopy shaking, we choose the initial shaking phase to avoid the jump. The jump in velocity scales as $1/\omega_{\mathrm{sp}}$ and is therefore most pronounced at small spectroscopy frequencies of 100 Hz. The initial jump leads to an additional velocity of the atoms in the lattice, which in principle can be sensitive to the dependence of the Floquet eigenstates on quasimomentum. The coefficient of the $1/\omega_{\mathrm{sp}}$ term is indeed larger in the non-trivial region, but within statistical errors

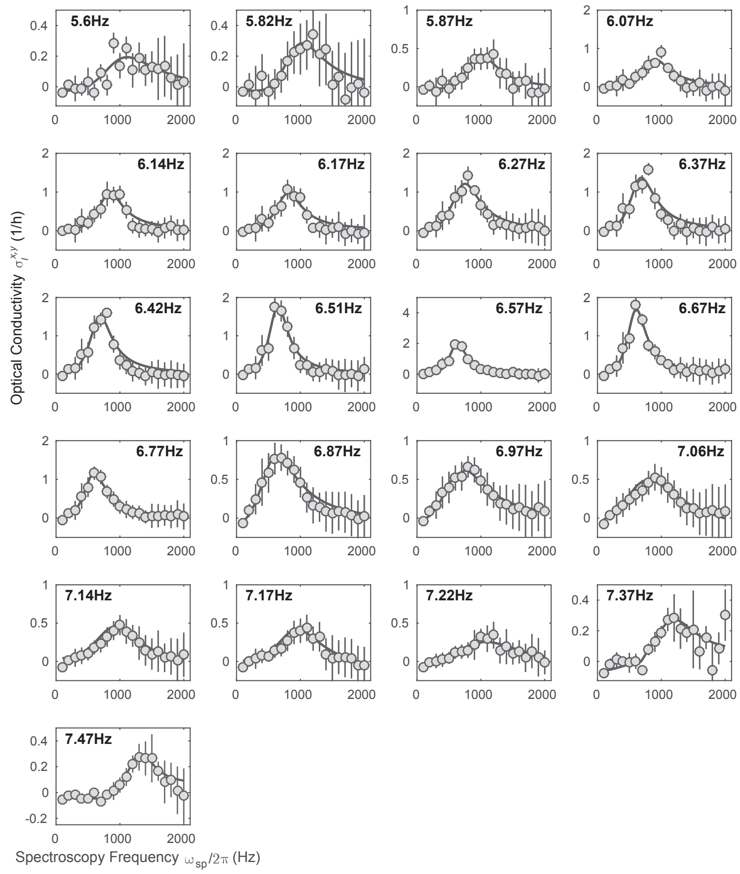

FIG. S5. **Optical conductivity of a topological system**. Optical conductivity curves obtained from the chiral spectra according to Eq. (2) of the main text). The number in the subfigures states the Floquet frequency $\omega_{\text{Fl}}/2\pi$. All errorbars denote the statistical uncertainty obtained by numerical propagation of the error on the depletion rates.

always equal for the two chiralities.

To obtain the frequency-integrated differential depletion rates, we determine the area under the fits as $A = \int_{\omega_0}^{\omega_1} \mathrm{d}\omega_{\text{sp}} \left(\frac{a}{\pi\gamma} \frac{1}{1+[(\omega_{\text{sp}}-\omega_0)/\gamma]^2} + c \right)$ with $\omega_0 = 2\pi \cdot 100\,\text{Hz}$ and $\omega_1 = 2\pi \cdot 2\,\text{kHz}$ corresponding to the range of experimentally probed frequencies. We only use the Lorentzian part of the fit in order to remove the contribution of the $1/\omega_{\text{sp}}$ term. As this heating feature is not part of the topological response and independent of the chirality of the spectroscopy drive, it cancels when calculating the differential rate. Using the fit in the determination of the area allows to reduce experimental noise.

We performed numerical calculations to deepen our understanding of the smooth behavior of the dichroic signal across the topological phase transition. In Fig. S7, we plot the data from

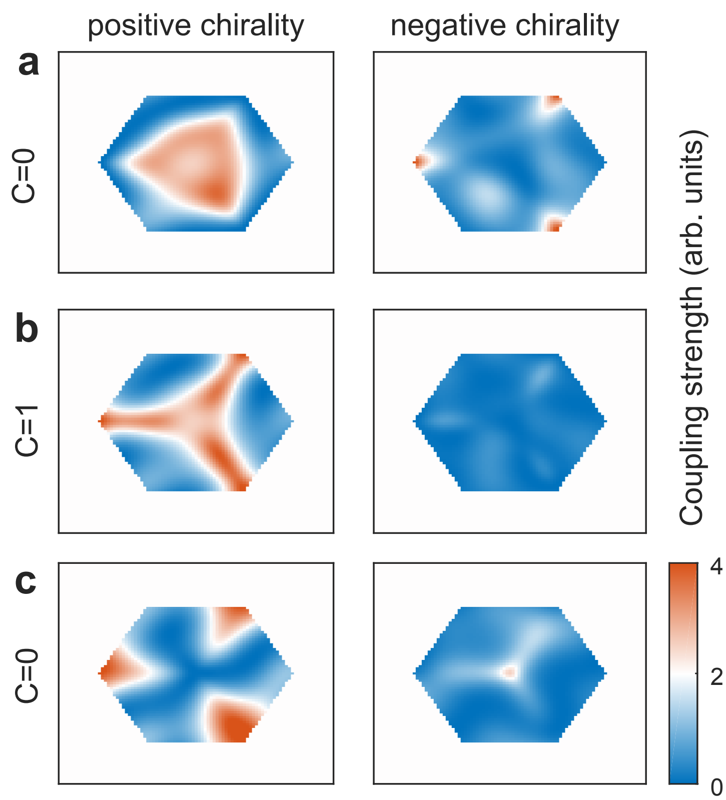

FIG. S6. **Numerical matrix elements of the drive between the two Floquet bands**. The matrix elements are evaluated for positive chirality (left) and negative chirality (right) of the perturbation. The Floquet bands are created by driving with negative chirality. The Floquet frequencies are $\omega_{\mathbf{Fl}} = 2\pi \cdot 5.9\,\mathrm{kHz}$ (C=0)(a), $\omega_{\mathbf{Fl}} = 2\pi \cdot 6.6\,\mathrm{kHz}$ (C=1)(b), and $\omega_{\mathbf{Fl}} = 2\pi \cdot 7.0\,\mathrm{kHz}$ (C=0)(c).

Fig. 4**a** of the main text together with the signal obtained by integrating the numerical spectra from Fig. S2 with different lower cutoffs in the integration. For a cutoff of 200 Hz, the numerical curve is smoothened and partially captures the smooth behavior of the data. The lower cutoff is motivated by the fact that the heating feature in the data can hide the dichroic signal at low frequencies.

SPECTROSCOPY OF A FLOQUET SYSTEM: TIME-SCALE SEPARATION AND MICRO-MOTION

In our experiment, we probe the properties of a Floquet-engineered system through a spectroscopic measurement. In this setting, the total system contains two types of time-dependent features: (a) the Floquet drive ('Fl') used to engineer a band structure of interest, and (b) the time-

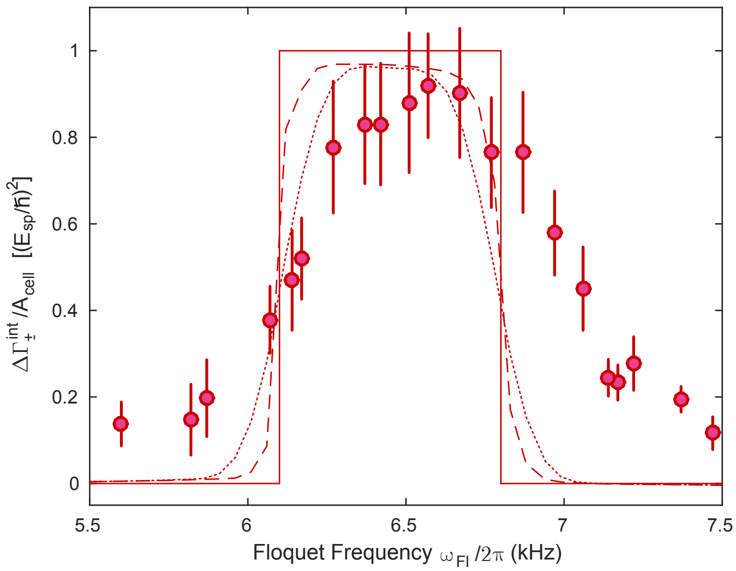

FIG. S7. **Dichroic signal across the topological phase diagram**. Measured dichroic signal (from Fig. 4**a** of the main text) together with the signal obtained by integrating the numerical spectra from Fig. S2. The lower cutoffs in the integration of the numerical spectra was 100 Hz (dashed line) and 200 Hz (dotted line). For comparison, the ideal step-like response is also plotted (solid line). All errorbars denote the statistical uncertainty obtained by numerical propagation of the error on the depletion rates.

dependent perturbation ('sp') that is used as a spectroscopic probe. It is the aim of this theory Section to explore the interplay between these two crucial features of our experimental setting. In the following, we set $\hbar = 1$ unless otherwise stated.

Basics of Floquet engineering Floquet engineering consists in modifying the properties of a system by subjecting it to a time-periodic drive [S16–S18]. The corresponding Hamiltonian can thus be written in the general form

$$\hat{H}(t) = \hat{H}_0 + \hat{V}_{\mathrm{Fl}}(t), \quad \hat{V}_{\mathrm{Fl}}(t + T_{\mathrm{Fl}}) = \hat{V}_{\mathrm{Fl}}(t), \tag{S1}$$

where $\hat{H}_0$ is a static Hamiltonian, and where $T_{\mathrm{Fl}} = 2\pi/\omega_{\mathrm{Fl}}$ is the period of the drive. Since the system is time-periodic, its stroboscopic dynamics – probed at times multiple of the period T – can be generated by the time-evolution operator over a single period $\hat{U}(T)$. Specifically, the state of the system at time $t_N = NT$ is obtained as $|\psi(t_N)\rangle = [\hat{U}(T)]^N|\psi(0)\rangle$, where $|\psi(0)\rangle$ denotes the initial state at time $t = 0$. When writing the time-evolution operator in the appealing form $\hat{U}(T) = \exp(-iT\hat{H}_{\mathrm{eff}})$, one can write the time-evolved state as $|\psi(t_N)\rangle = \exp(-it_N\hat{H}_{\mathrm{eff}})|\psi(0)\rangle$, which indicates that the system evolves as if it was described by a time-independent effective

Hamiltonian $\hat{H}_{\text{eff}}$. In general, the latter is a complicated operator, which stems from a rich interplay between the static Hamiltonian $\hat{H}_0$ and the drive $\hat{V}_{\text{Fl}}(t)$, and it can be explicitly computed using the methods of Refs. [S18–S21]. Importantly, the discussion above builds on a stroboscopic-evolution picture, and in this sense, it disregards the effects of micro-motion (i.e. the evolution at intermediate times $t_N \neq NT$). These micro-motion effects can also be systematically studied, using the formalism of Refs. [S18, S19].

The simplified picture and the hierarchy of scales In the experiment, we are interested in probing the properties of an effective Hamiltonian $\hat{H}_{\text{eff}}$, which results from a Floquet-engineering protocol, as explained above. In analogy with the spectroscopy of static systems, we act on the Floquet-engineered system with an extra time-dependent perturbation, so that the corresponding (total) Hamiltonian can be loosely written as

$$\hat{\mathfrak{H}}_{\text{tot}}(t) = \hat{H}_{\text{eff}} + \hat{V}_{\text{sp}}(t), \quad \hat{V}_{\text{sp}}(t + T_{\text{sp}}) = \hat{V}_{\text{sp}}(t), \tag{S2}$$

where $\hat{V}_{\text{sp}}(t)$ describes the effects of the spectroscopic probe, and where we assumed that the Floquet-engineered system can be treated as a static system captured by the effective Hamiltonian $\hat{H}_{\text{eff}}$. Importantly, the latter simplification should be treated with care, as we will investigate in more detail below. Intuitively, this approach should hold whenever the system presents a clear separation of time-scales: Introducing the bandwidth of the effective spectrum, W_{eff}, one typically has the hierarchy of scales,

$$\omega_{\text{sp}} \lesssim W_{\text{eff}} \ll \omega_{\text{Fl}}, \tag{S3}$$

where $\omega_{\text{sp}} = 2\pi/T_{\text{sp}}$ denotes the probe frequency. Indeed, Floquet-engineering typically operates in the so-called "high-frequency regime", where $\hbar\omega_{\text{Fl}} \to \infty$ sets the largest energy scale in the problem [S16, S18]. When the hierarchy in Eq. (S3) is satisfied, one expects the micro-motion effects to be irrelevant, which justifies the simplification introduced in Eq. (S2).

Probing Floquet systems: A numerical study It is the aim of this Section to analyze the validity of this probing approach, by studying the full time-dependent Hamiltonian, i.e. the total Hamiltonian that explicitly contains the two types of time-dependent features, namely,

$$\hat{H}_{\text{tot}}(t) = \hat{H}_0 + \hat{V}_{\text{Fl}}(t) + \hat{V}_{\text{sp}}(t), \tag{S4}$$

where both the Floquet drive and the probe are explicitly written, i.e. without applying the aforementioned simplification [Eq. (S2)]. In our experiment, $\hat{H}_0$ describes the motion of a particle in a 2D honeycomb lattice with large energy offsets between neighboring sites, while both $\hat{V}_{\text{Fl}}(t)$ and

$\hat{V}_{\rm sp}(t)$ describe the effects of circular shaking; we note that the corresponding frequencies $\omega_{\rm sp}$ and $\omega_{\rm Fl}$ indeed satisfy the hierarchy in Eq. (S3); see main text. In our setting, the effective Hamiltonian $\hat{H}_{\rm eff}$ is reminiscent of the Haldane model [S3], i.e. a two-band lattice model displaying Bloch bands with non-zero Chern numbers. The corresponding Hamiltonian can thus be written in the momentum representation as

$$\hat{H}_{\rm eff}(\mathbf{q}) = d_x(\mathbf{q})\hat{\sigma}_x + d_y(\mathbf{q})\hat{\sigma}_y + d_z(\mathbf{q})\hat{\sigma}_z, \tag{S5}$$

where $\mathbf{q}$ denotes the quasi-momentum and $\hat{\sigma}_{x,y,z}$ are the Pauli matrices reflecting the pseudo-spin structure associated with the honeycomb lattice. Following the proposal in Ref. [S2], the Chern number of the lowest band $\varepsilon_-(\mathbf{q}) = -(d_x^2+d_y^2+d_z^2)^{1/2}$, can be probed by subjecting the Haldane model to a circular drive and by measuring the resulting excitation rates (see also the main text); this circular perturbation corresponds to the spectroscopic probe $\hat{V}_{\rm sp}(t)$ in Eq. (S4).

When treated in a proper frame [S2], the circular drives [$\hat{V}_{\rm Fl}(t)$ and $\hat{V}_{\rm sp}(t)$] enter the Hamiltonian in Eq. (S4) as a uniform time-dependent gauge potential that affects the hopping terms in $\hat{H}_0$; hence, these time-dependent features do not affect the translational symmetry of the problem. Consequently, the total Hamiltonian in Eq. (S4) still decouples in terms of the quasi-momenta, which results in a set of driven two-level systems (one for each quasi-momentum $\mathbf{q}$):

$$\hat{H}_{\rm tot}(\mathbf{q};t) = \varepsilon(\mathbf{q})\hat{1} + d_x(\mathbf{q};t)\hat{\sigma}_x + d_y(\mathbf{q};t)\hat{\sigma}_y + d_z(\mathbf{q})\hat{\sigma}_z. \tag{S6}$$

In order to explore the interplay between the different types of time-modulations [$\hat{V}_{\rm Fl}(t)$ and $\hat{V}_{\rm sp}(t)$], we now consider a similar but simpler model: a time-modulated two-level system described by the Hamiltonian:

$$\begin{aligned}
&\hat{H}(t) = \hat{H}_0 + \hat{V}_{\rm Fl}(t) + \hat{V}_{\rm sp}(t), \qquad\qquad (S7)\\
&\hat{H}_0 = \Delta|1\rangle\langle 1| + J\left(|0\rangle\langle 1| + |1\rangle\langle 0|\right),\\
&\hat{V}_{\rm Fl}(t) = K_{\rm Fl}\cos(\Delta t)|0\rangle\langle 0|, \quad \hat{V}_{\rm sp}(t) = 4K_{\rm sp}\cos(\omega_{\rm sp}t)|0\rangle\langle 0|,
\end{aligned}$$

which is indeed a direct analog of our experimental shaken optical lattice: the two levels (or 'sites') are separated by a large offset $\Delta \gg J$, and the effective coupling is reintroduced by the resonant time-modulation $\hat{V}_{\rm Fl}(t)$, i.e. $\omega_{\rm Fl} = \Delta$. In the absence of the probe ($K_{\rm sp} = 0$), the dynamics is well described by the effective Hamiltonian [S19]

$$\hat{H}_{\rm eff} = J\mathscr{J}_1(K_{\rm Fl}/\Delta)\left(|0\rangle\langle 1| + |1\rangle\langle 0|\right) + \mathscr{O}(1/\Delta), \tag{S8}$$

where $\mathscr{J}_1$ is a Bessel function of first kind; this is the basic mechanism for photon-assisted tunneling [S16]. The perturbation $\hat{V}_{\rm sp}(t)$ is then introduced to probe the effective system characterized by $\hat{H}_{\rm eff}$. Importantly, we note that the operators associated with both the Floquet-drive and the probe commute with each other, $[\hat{V}_{\rm Fl}, \hat{V}_{\rm sp}]=0$, which is also the case in our experiment (since both effects are generated by circular shaking); this aspect will be further discussed at the end of this Section.

Let us assume for now that the system can be simplified in the 'ideal' (or naive) form in Eq. (S2), namely, let us assume that the Floquet-engineered system can indeed be treated as a static (effective) Hamiltonian, as given in Eq. (S8). For convenience, we now introduce the eigenstates of the effective (Floquet) Hamiltonian:

$$|+\rangle = (1/\sqrt{2})\,(|0\rangle + |1\rangle)\,, \qquad |-\rangle = (1/\sqrt{2})\,(|0\rangle - |1\rangle)\,,$$

which will be referred to as "dressed states" in the following. Their energies are $\varepsilon_\pm = \pm J\,\mathscr{J}_1(K_{\rm Fl}/\Delta)$, according to Eq. (S8). In this "dressed-state" basis, the ideal Hamiltonian in Eq. (S2) now explicitly reads

$$\hat{\mathfrak{H}}_{\rm tot}(t) = J\,\mathscr{J}_1(K_{\rm Fl}/\Delta)\hat{\sigma}_z + 2K_{\rm sp}\cos(\omega_{\rm sp}t)\left(\hat{\sigma}_x + \hat{1}\right). \tag{S9}$$

From this, one may propose the following probing protocol: Setting the probe frequency on resonance with respect to the energy separation, $\omega_{\rm sp} = \varepsilon_+ - \varepsilon_- = 2J\,\mathscr{J}_1(K_{\rm Fl}/\Delta)$, and assuming that the lowest-energy dressed-state is initially occupied $|\langle -|\psi(t=0)\rangle|^2 = 1$, should result in perfect Rabi oscillations between the two dressed states. Furthermore, extracting the excitation rate Γ at short times compared to the Rabi period ($t \ll 1/K_{\rm sp}$), and integrating over the probe frequency should verify the relation [S2, S22]

$$\int_0^\infty \Gamma(\omega_{\rm sp})\mathrm{d}\omega_{\rm sp} \approx 2\pi|\langle +|\hat{V}_{\rm sp}^+|-\rangle|^2 = 2\pi K_{\rm sp}^2, \tag{S10}$$

where $\hat{V}_{\rm sp}^+$ is defined through $\hat{V}_{\rm sp}(t) = \hat{V}_{\rm sp}^+ e^{-i\omega_{\rm sp}t} + \hat{V}_{\rm sp}^- e^{i\omega_{\rm sp}t}$; we point out that the relation in Eq. (S10) is only strictly valid within the rotating-wave-approximation, $t \gg 1/\omega_{\rm sp}$, where anti-resonant contributions can be safely neglected (note that this approximation breaks down in the limit of an arbitrarily small energy separation, $J\,\mathscr{J}_1(K_{\rm Fl}/\Delta) \sim \omega_{\rm sp} \to 0$; see discussion below). Importantly, the relation (S10) between the integrated excitation rate and the coupling matrix element $|\langle +|\hat{V}_{\rm sp}^+|-\rangle|^2$ is at the core of the quantized dichroism effect revealed in the experiment; see Ref. [S2, S22] for details.

We now numerically explore this protocol, to test the validity of this spectroscopic approach. For practical reasons, we study this scenario in a different frame, as generated by the unitary operator [S19]

$$\hat{R}(t) = \exp\left[i\Delta t|1\rangle\langle 1| + i(K_{\text{Fl}}/\Delta)\sin(\Delta t)|0\rangle\langle 0|\right]. \tag{S11}$$

In this frame, the total Hamiltonian in Eq. (S7) now reads

$$\begin{aligned}\mathscr{H}(t) &= \hat{R}\hat{H}(t)\hat{R}^\dagger - i\hat{R}\partial_t\hat{R}^\dagger \\ &= J|0\rangle\langle 1|\exp\left[i(K_{\text{Fl}}/\Delta)\sin(\Delta t) - i\Delta t\right] + \text{h.c.} \\ &+ 4K_{\text{sp}}\cos(\omega_{\text{sp}}t)|0\rangle\langle 0|.\end{aligned} \tag{S12}$$

This is the Hamiltonian that we implement numerically in our time-evolution simulations discussed below. One should note that this Hamiltonian includes all the time-dependences of our problem (i.e. there are no approximation at this level).

Before presenting the numerics, let us discuss the different energy scales. In the following, we set $J = 1$ to be our unit of energy, and we also set $K_{\text{Fl}}/\Delta = 2$ such that $\omega_{\text{sp}} = 2J\mathscr{J}_1(K_{\text{Fl}}/\Delta) \approx 1$. In this situation, a good separation of energy scales is obtained for $\Delta \gg 1$: the Floquet and probe frequencies satisfy $\omega_{\text{Fl}} \gg \omega_{\text{sp}}$. Hence, deviations from the ideal situation [Eq. (S2)] are expected for $\Delta \sim 1$. In the following, we also set the perturbation strength $K_{\text{sp}} = 0.01J$ in order to have relatively long Rabi periods.

We show in Fig. S8 the excited fraction $N_{\text{ex}}(t)$, i.e. the occupation in the high-energy dressed state, for various values of Δ. Here, the dressed states $|+,-\rangle$ are obtained as the eigenstates of the exact effective Hamiltonian (evaluated numerically), and the probe frequency ω_{sp} is adjusted so as to match the energy difference between them (this allows one to avoid any residual detuning effect). As shown in Fig. S8(a), the excited fraction depicts a perfect Rabi oscillation in the case of a large time-scale separation ($\Delta = 100J$). As Δ is reduced, one observes a clear manifestation of the micro-motion effects [Fig. S8(b)-(c)]. In the absence of time-scale separation [Fig. S8(d)], the Rabi oscillation is barely recognizable. Next, we calculate the spectrum $N_{\text{ex}}(\omega_{\text{sp}})$, for a fixed probing time t_{obs} that is small compared to the Rabi period, i.e. $t_{\text{obs}} \ll 1/K_{\text{sp}}$. In order to highlight the effects of micro-motion, we compare the spectra obtained for stroboscopic and non-stroboscopic times (with respect to the Floquet period T_{Fl}). The spectra shown in Fig. S9(a) for $\Delta = 100J$ reveal the well-know sinc-squared function associated with the Rabi formula [S23], and the micro-motion effect is essentially invisible. This is no longer the case for the smaller value $\Delta = 10J$, where the spectra obtained for stroboscopic and non-stroboscopic times are found to slightly differ. Finally, we test the relation in Eq. (S10) by measuring the quantity

$$\mathfrak{N} = (1/2\pi K_{\rm sp}^2)\int_{\omega_{\rm cut}}^{\bar{\omega}_{\rm cut}} \Gamma(\omega_{\rm sp}){\rm d}\omega_{\rm sp}, \tag{S13}$$

where the rate is obtained as $\Gamma(\omega_{\rm sp}) = N_{\rm ex}(\omega_{\rm sp})/t_{\rm obs}$, and where we set the cut-offs at $\omega_{\rm cut} = 0.5J$ and $\bar{\omega}_{\rm cut} = 2.5J$ (see Fig. S9). Within the regime of validity of Eq. (S10), we expect the "marker" in Eq. (S13) to be quantized $\mathfrak{N} = 1$ in the limit of infinite time-scale separation. From the spectra in Fig. S9, we obtain

$$\Delta = 100J: \quad \mathfrak{N} = 0.96 \text{ for } t_{\rm obs}^{\rm strob}, \quad \mathfrak{N} = 0.93 \text{ for } t_{\rm obs}^{\text{non-strob}},$$
$$\Delta = 10J: \quad \mathfrak{N} = 0.95 \text{ for } t_{\rm obs}^{\rm strob}, \quad \mathfrak{N} = 1.13 \text{ for } t_{\rm obs}^{\text{non-strob}},$$

where $t_{\rm obs}^{\rm strob}$ and $t_{\rm obs}^{\text{non-strob}}$ refer to the stroboscopic and non-stroboscopic observation times. This shows that for $\Delta = 10J$, an error of about 10% can be attributed to the micro-motion; we note that this error can be reduced by optimizing the cut-offs.

As already mentioned above, the relation in Eq. (S10) is only strictly valid within the rotating-wave-approximation, which assumes that the observation time t verifies $t \gg 1/\Delta_{\rm gap}$, where $\Delta_{\rm gap} = 2J\mathscr{J}_1(K_{\rm Fl}/\Delta)$ denotes the energy separation between the two levels (we used the resonance condition $\omega_{\rm sp} = \Delta_{\rm gap}$). Consequently, the quantization of the marker $\mathfrak{N}$ breaks down in the limit of an arbitrarily small gap $\Delta_{\rm gap} \to 0$. This effect is illustrated in Fig. S10, which shows the measured marker $\mathfrak{N}$ as a function of the effective energy gap $\Delta_{\rm gap}$; these results were obtained by measuring the integrated excitation rates for different values of the ratio $K_{\rm Fl}/\Delta$. The curve $\mathfrak{N}(\Delta_{\rm gap})$ presented in Fig. S10 shows a smooth falloff of the marker as one reduces the size of the gap. This behavior is inherent to the present spectroscopic approach, which relies on the rotating-wave-approximation. This analysis of the two-level system offers a simple explanation for the behavior of the extracted Chern number across the topological phase transition (where the spectral gap of the 2-band model closes) presented in the main text; see Fig. 4.

Effect of time modulations with non-commuting operators In the previous subsection, we considered the case where the Floquet drive $\hat{V}_{\rm Fl}(t)$ and the probe $\hat{V}_{\rm sp}(t)$ commute with each other, which is also the case in the experiment described in the main text (where both drives correspond to a circular shake of the lattice). In this paragraph, we briefly discuss a subtlety that arises when treating a more generic situation where the two drives do not commute.

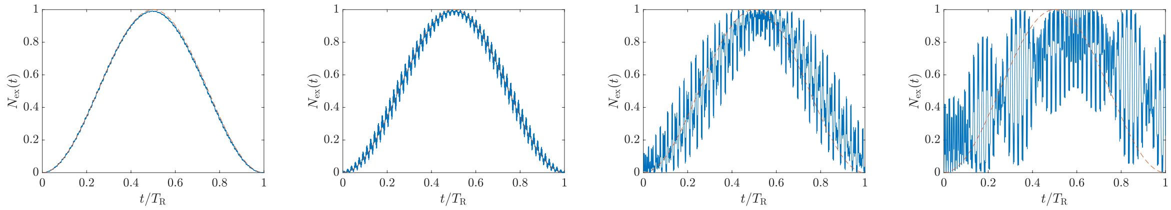

(a) $\Delta = 100J$ (b) $\Delta = 10J$ (c) $\Delta = 3J$ (d) $\Delta = 2J$

FIG. S8. Excited fraction $N_{\text{ex}}(t)$, i.e. the occupation in the high-energy dressed state over time, for various values of the initial detuning: $\Delta = 100J$, $\Delta = 10J$, $\Delta = 3J$ and $\Delta = 2J$. The thin red dotted line shows the perfect Rabi oscillation, as predicted by the simplified approach [Eq. (S2)], i.e. neglecting the micro-motion effects. The time-evolution shown by the blue curves is numerically generated from the full time-dependent Hamiltonians in Eqs. (S12). The parameters are: $K_{\text{Fl}} = 2\Delta$, $K_{\text{sp}} = 0.01J$ and the probe frequency ω_{sp} is adjusted so as to match the energy difference between the eigenstates of the exact effective Hamiltonian $\hat{H}_{\text{eff}}$ (as evaluated numerically). Time is expressed in units of the Rabi period: $T_R = \pi/K_{\text{sp}}$.

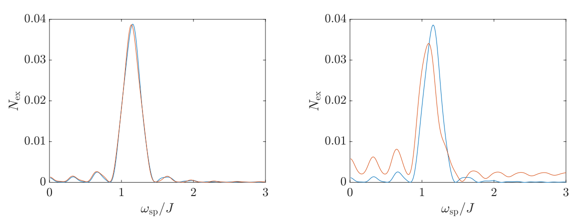

(a) $\Delta = 100J$ (b) $\Delta = 10J$

FIG. S9. Excited fraction $N_{\text{ex}}(\omega_{\text{sp}})$ as a function of the probe frequency for $\Delta = 100J$ and $\Delta = 10J$. The spectra are obtained for stroboscopic (blue curve) and non-stroboscopic (red curves) observation times with respect to the Floquet period T_{Fl}. These times are chosen to be small compared to the Rabi period: $t_{\text{obs}}^{\text{strob}} = 0.062T_R$ and $t_{\text{obs}}^{\text{non-strob}} = 0.0637T_R$. Note that $t_{\text{obs}}^{\text{strob}} = 0.062T_R$ corresponds to $31T_{\text{Fl}}$ (for $\Delta = 10$) and $310T_{\text{Fl}}$ (for $\Delta = 100$).

To do so, we now modify the driven two-level system in Eq. (S7) in a minimal manner by

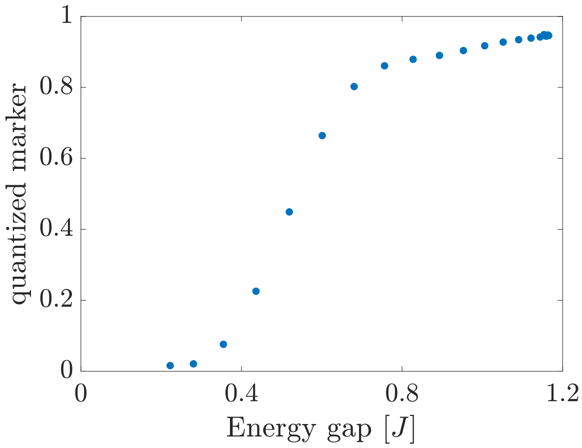

FIG. S10. Quantized marker $\mathfrak{N}(\Delta_{\mathrm{gap}})$ defined in Eq. (S13) as a function of the effective energy separation in the driven two-level system. This plot illustrates the breakdown of the rotating-wave approximation upon reducing the size of the gap (i.e. as one decreases the ratio K_{Fl}/Δ). The parameters are the same as in Fig. S9.

considering the time-dependent Hamiltonian

$$\begin{aligned}\hat{H}(t) &= \hat{H}_0 + \hat{V}_{\mathrm{Fl}}(t) + \hat{\mathscr{V}}_{\mathrm{sp}}(t), \\ \hat{H}_0 &= \Delta|1\rangle\langle 1| + J\left(|0\rangle\langle 1| + |1\rangle\langle 0|\right), \\ \hat{V}_{\mathrm{Fl}}(t) &= K_{\mathrm{Fl}}\cos(\Delta t)|0\rangle\langle 0|, \\ \hat{\mathscr{V}}_{\mathrm{sp}}(t) &= 2K_{\mathrm{sp}}\cos(\omega_S t)(-i|0\rangle\langle 1| + i|1\rangle\langle 0|).\end{aligned} \tag{S14}$$

In contrast with the probe operator $\hat{V}_{\mathrm{sp}}(t)$ in Eq. (S7), the two drives entering the problem no longer commute with each other: $[\hat{V}_{\mathrm{Fl}}, \hat{\mathscr{V}}_{\mathrm{sp}}] \neq 0$.

If one naively follows the simplified approach [Eq. (S2)], one recovers the analogue of Eq. (S9),

$$\hat{\mathfrak{H}}_{\mathrm{tot}}(t) = J\,\mathscr{J}_1(K_{\mathrm{Fl}}/\Delta)\hat{\sigma}_z - 2K_{\mathrm{sp}}\cos(\omega_{\mathrm{sp}}t)\hat{\sigma}_y, \tag{S15}$$

where we simply added the new probe $\hat{\mathscr{V}}_{\mathrm{sp}}(t)$ on top of the effective Hamiltonian $\hat{H}_{\mathrm{eff}}$ in Eq. (S8), both expressed in the dressed-state basis. The expression in Eq. (S15) justifies the choice of the new perturbation $\hat{\mathscr{V}}_{\mathrm{sp}}(t)$ in Eq. (S14): Similarly to $\hat{V}_{\mathrm{sp}}(t)$ in Eq. (S7), the probe $\hat{\mathscr{V}}_{\mathrm{sp}}(t)$ is predicted to generate Rabi oscillations between the two dressed states upon setting the probe frequency ω_{sp} on resonance.

However, the above observation is not complete. Indeed, more care is required in this non-commutative context, as we now explain. As in the previous subsection, let us consider the frame

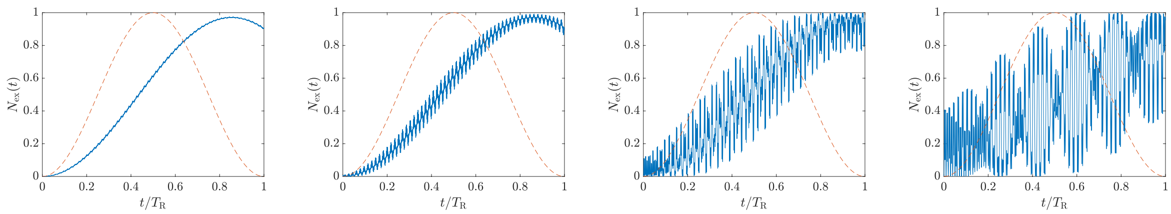

(a) $\Delta = 100J$ (b) $\Delta = 10J$ (c) $\Delta = 3J$ (d) $\Delta = 2J$

FIG. S11. Excited fraction $N_{\mathrm{ex}}(t)$, i.e. the occupation in the high-energy dressed state over time, using the non-commutating probe $\hat{\mathscr{V}}_{\mathrm{Sp}}(t)$ in Eq. (S14), and for various values of the initial detuning: $\Delta = 100J$, $\Delta = 10J$, $\Delta = 3J$ and $\Delta = 2J$. The thin red dotted line shows the Rabi oscillation, as predicted by the over-simplified approach [Eq. (S15)], i.e. neglecting the non-commutativity effects. The time-evolution shown by the blue curves is numerically generated from the full time-dependent Hamiltonians in Eq. (S16), respectively. The parameters are: $K_{\mathrm{Fl}} = 2\Delta$, $K_{\mathrm{sp}} = 0.01J$ and the probe frequency ω_{sp} is adjusted so as to match the energy difference between the eigenstates of the exact effective Hamiltonian $\hat{H}_{\mathrm{eff}}$ (as evaluated numerically). Time is expressed in units of the (naive) Rabi period: $T_R = \pi/K_{\mathrm{sp}}$.

transformation generated by the operator $\hat{R}(t)$ in Eq. (S11), and let us write the full time-dependent Hamiltonian (S14) in this new frame,

$$\begin{aligned}\mathscr{H}(t) &= \hat{R}\hat{H}(t)\hat{R}^{\dagger} - i\hat{R}\partial_t\hat{R}^{\dagger} \\ &= J|0\rangle\langle 1|\exp\left[i(K_{\mathrm{Fl}}/\Delta)\sin(\Delta t) - i\Delta t\right] + \text{h.c.} \\ &- 2iK_{\mathrm{sp}}\cos(\omega_{\mathrm{sp}}t)|0\rangle\langle 1|\exp\left[i(K_{\mathrm{Fl}}/\Delta)\sin(\Delta t) - i\Delta t\right] + \text{h.c.}\end{aligned} \tag{S16}$$

In the presence of time-scale separation $T_{\mathrm{sp}} \gg T_{\mathrm{Fl}}$, one can approximate the problem by performing a time-average of the Hamiltonian in Eq. (S16) over a period T_{Fl}, while maintaining the time-dependence of the slow function $\cos(\omega_{\mathrm{sp}}t)$. This more rigorous approach yields the effective time-dependent Hamiltonian

$$\hat{\mathfrak{H}}_{\mathrm{tot}}(t) = \mathscr{J}_1(K_{\mathrm{Fl}}/\Delta)\left\{J\hat{\sigma}_z - 2K_{\mathrm{sp}}\cos(\omega_{\mathrm{sp}}t)\hat{\sigma}_y\right\}, \tag{S17}$$

which is similar to the more 'naive' Hamiltonian in Eq. (S15), except that the coupling matrix elements are now renormalized by the Bessel function: $K_{\mathrm{sp}} \to \mathscr{J}_1(K_{\mathrm{Fl}}/\Delta)K_{\mathrm{sp}}$. Consequently, the Rabi frequency characterizing the resulting Rabi oscillations is reduced by a factor $\mathscr{J}_1(K_{\mathrm{Fl}}/\Delta)$, with respect to the case of the commutating probe $\hat{V}_{\rm sp}$. This observation is subtle, but crucial, whenever one probes a system with a non-commutating probe operator in view of extracting the coupling matrix elements entering Eq. (S10), e.g. to extract the Chern number [S2, S22].

We validate this result in Fig. S11, where we plot the analogue of Fig. S8 now for the non-commutating probe $\hat{\mathscr{V}}_{\rm sp}$. Here, one clearly visualizes a striking elongation of the Rabi period T_R corresponding to the factor $1/\mathscr{J}_1(K_{\rm Fl}/\Delta) \approx 1.73$, as predicted above. Besides, we note that the micro-motion effects that appear as one decreases the value of Δ are slightly enhanced as compared to the commutative case [Fig. S8]. Most importantly, this renormalization of the Rabi frequency strongly modifies the integrated rate relation in Eq. (S10). To see this, we now calculate the following quantity

$$\mathfrak{N}_{\rm renorm} = [1/2\pi(\mathscr{J}_1(K_{\rm Fl}/\Delta)K_{\rm sp})^2] \int_{\omega_{\rm cut}}^{\bar{\omega}_{\rm cut}} \Gamma(\omega_{\rm sp}) {\rm d}\omega_{\rm sp}, \tag{S18}$$

which differs from the marker in Eq. (S13) in that $\mathfrak{N}_{\rm renorm}$ explicitly takes into account the renormalized Rabi frequency, i.e. $K_{\rm sp} \to \mathscr{J}_1(K_{\rm Fl}/\Delta)K_{\rm sp}$. From our numerical simulations, we obtain $\mathfrak{N}_{\rm renorm} = 1.02$ for $\Delta = 100J$ and $\mathfrak{N}_{\rm renorm} = 1.20$ for $\Delta = 10J$ (using the same parameters as above). This numerical analysis illustrates how probing Floquet systems should be treated with care, when using spectroscopic probes that do not commute with the Floquet drive. We point out that while these effects do not affect the experiment discussed in the main text (where both drives commute with each other), we anticipate that they might play a role in other Floquet-based experimental settings.

* klaus.sengstock@physnet.uni-hamburg.de

[S1] Fläschner, N. *et al.* Experimental reconstruction of the Berry curvature in a Floquet Bloch band. *Science* **352**, 1091–1094 (2016).

[S2] Tran, D. T., Dauphin, A., Grushin, A. G., Zoller, P. & Goldman, N. Probing topology by "heating": Quantized circular dichroism in ultracold atoms. *Science Advances* **3**, e1701207 (2017).

[S3] Haldane, F. D. M. Model for a Quantum Hall Effect without Landau Levels: Condensed-Matter Realization of the Parity Anomaly. *Phys. Rev. Lett.* **61**, 2015 (1988).

[S4] Oka, T. & Aoki, H. Photovoltaic Hall effect in graphene. *Phys. Rev. B* **79**, 081406(R) (2009).

[S5] Zheng, W. & Zhai, H. Floquet topological states in shaking optical lattices. *Phys. Rev. A* **89**, 061603(R) (2014).

[S6] Jotzu, G. *et al.* Experimental realisation of the topological Haldane model with ultracold fermions. *Nature* **515**, 237–240 (2014).

[S7] Tarnowski, M. *et al.* Characterizing topology by dynamics: Chern number from linking number. *arXiv:1709.01046* (2017).

[S8] Marzari, N. & Vanderbilt, D. Maximally localized generalized wannier functions for composite energy bands. *Phys. Rev. B* **56**, 12847 (1997).

[S9] Ozawa, T. & Goldman, N. Extracting the quantum metric tensor through periodic driving. *Phys. Rev. B* **97**, 201117(R) (2018).

[S10] Thonhauser, T. & Vanderbilt, D. Insulator/Chern-insulator transition in the Haldane model. *Phys. Rev. B* **74**, 235111 (2006). 0608527.

[S11] Yao, W., Xiao, D. & Niu, Q. Valley Dependent Optoelectronics from Inversion Symmetry Breaking. *Phys. Rev. B* **77**, 235406 (2008).

[S12] Buchhold, M., Cocks, D. & Hofstetter, W. Effects of smooth boundaries on topological edge modes in optical lattices. *Phys. Rev. A* **85**, 063614 (2012). 1204.0016.

[S13] Goldman, N., Beugnon, J. & Gerbier, F. Identifying topological edge states in 2d optical lattices using light scattering. *The European Physical Journal Special Topics* **217**, 135–152 (2013).

[S14] Aidelsburger, M. *et al.* Measuring the Chern number of Hofstadter bands with ultracold bosonic atoms. *Nature Phys.* **11**, 162–166 (2015).

[S15] Heinze, J. *et al.* Intrinsic photoconductivity of ultracold fermions in optical lattices. *Phys. Rev. Lett.* **110**, 085302 (2013).

[S16] Eckardt, A. Colloquium: Atomic quantum gases in periodically driven optical lattices. *Rev. Mod. Phys.* **89**, 011004 (2017).

[S17] Cayssol, J., Dóra, B., Simon, F. & Moessner, R. Floquet topological insulators. *physica status solidi (RRL)-Rapid Research Letters* **7**, 101–108 (2013).

[S18] Goldman, N. & Dalibard, J. Periodically driven quantum systems: effective hamiltonians and engineered gauge fields. *Phys. Rev. X* **4**, 031027 (2014).

[S19] Goldman, N., Dalibard, J., Aidelsburger, M. & Cooper, N. Periodically driven quantum matter: The case of resonant modulations. *Phys. Rev. A* **91**, 033632 (2015).

[S20] Eckardt, A. & Anisimovas, E. High-frequency approximation for periodically driven quantum systems from a floquet-space perspective. *New J. Phys.* **17**, 093039 (2015).

[S21] Mikami, T. *et al.* Brillouin-wigner theory for high-frequency expansion in periodically driven systems: Application to floquet topological insulators. *Phys. Rev. B* **93**, 144307 (2016).

[S22] Tran, D. T., Cooper, N. R. & Goldman, N. Quantized Rabi Oscillations and Circular Dichroism in Quantum Hall Systems. *Phys. Rev. A* **97**, 061602(R) (2018).

[S23] Cohen-Tannoudji, C., Laloe, F. & Diu, B. *Mécanique quantique*, vol. 3 (EDP Sciences, 2017).